

Research



Cite this article: Gillman A, Amadio G, Matouš K, Jackson TL. 2015 Third-order thermo-mechanical properties for packs of Platonic solids using statistical micromechanics. *Proc. R. Soc. A* **471**: 20150060. <http://dx.doi.org/10.1098/rspa.2015.0060>

Received: 28 January 2015

Accepted: 11 March 2015

Subject Areas:

mechanics, materials science, computational mathematics

Keywords:

heterogeneous materials, effective material properties, statistical micromechanics, adaptive interpolation/integration, high-performance computing

Author for correspondence:

K. Matouš

e-mail: kmatous@nd.edu

Third-order thermo-mechanical properties for packs of Platonic solids using statistical micromechanics

A. Gillman¹, G. Amadio², K. Matouš¹,
and T. L. Jackson³

¹Department of Aerospace and Mechanical Engineering, University of Notre Dame, Notre Dame, IN 46556, USA

²Department of Aerospace Engineering, University of Illinois, Urbana, IL 61801, USA

³Department of Aerospace and Mechanical Engineering, University of Florida, Gainesville, FL 32611, USA

Obtaining an accurate higher order statistical description of heterogeneous materials and using this information to predict effective material behaviour with high fidelity has remained an outstanding problem for many years. In a recent letter, Gillman & Matouš (2014 *Phys. Lett. A* **378**, 3070–3073. (doi:10.1016/j.physleta.2014.08.032)) accurately evaluated the three-point microstructural parameter that arises in third-order theories and predicted with high accuracy the effective thermal conductivity of highly packed material systems. Expanding this work here, we predict for the first time effective thermo-mechanical properties of granular Platonic solid packs using third-order statistical micromechanics. Systems of impenetrable and penetrable spheres are considered to verify adaptive methods for computing n -point probability functions directly from three-dimensional microstructures, and excellent agreement is shown with simulation. Moreover, a significant shape effect is discovered for the effective thermal conductivity of highly packed composites, whereas a moderate shape effect is exhibited for the elastic constants.

1. Introduction

Quantifying the morphology of many-body systems has applications in many scientific fields at a variety of length scales from molecular configurations [1,2] up to composite microstructures [3,4] and celestial bodies [5–7]. Often, these systems have varying degrees of randomness and can only be described through use of statistics. Moreover, the connection of a statistical description to observed physical phenomena has long been studied [3,8]. Bernal [9] first motivated the importance of higher order statistics when investigating the molecular arrangement of liquids using the radial distribution function. n -point probability functions were introduced by Frisch & Stillinger [10] to describe radiation scattering patterns in packs of voided media. Statistical characterization of many-body systems has remained prevalent as evidenced by more recent studies of the background cosmic radiation [6,11] and characterization of molecules in amorphous condensed matter (e.g. glasses [12]). Note that many-body systems are often spatially complex, and accurately obtaining higher order statistical descriptions in three dimensions have proved difficult.

The focus of this work is to predict effective transport and mechanical properties of particulate composites from higher order statistical data. This field has applications in many scientific and engineering disciplines including flow in fractured rock [13], design of structural composites [14] and use of conductive adhesives in electronics [15], just to name a few. Specifically, a primary objective of this work is to predict thermo-mechanical properties of highly filled crystalline packs (Platonic solids) and investigate the effect of the inclusion shape for a wide range of microstructures. Experimental observations for particular systems have shown significant shape effects. For example, Timofeeva *et al.* [16] show that alumina nanofluids have higher thermal conductivities for alumina particles with larger aspect ratios, and linear models dependent on the particle shape were developed. However, application of these linear models is limited to low particle concentrations. Direct numerical modelling of a shape effect was performed by Yvonnet *et al.* [17,18] for both mechanical and thermal properties. However, studies were limited to single particle simulations at low volume fractions. Chauhan *et al.* [19] developed a micromechanics model for the effective conductivity from a chain of single particle unit cells for various shapes. In [19], good agreement was obtained for some experiments at moderate particle volume fractions, but large errors were present for other tests.

Statistical micromechanics theories developed over the past half century have proved accurate for wide ranging particle concentrations. Brown [20] first used n -point probability functions to connect the microstructural details to the effective material behaviour. Hashin & Shtrikman [21] derived the most accurate second-order bounds for the permittivity/conductivity and elastic constants [22] for isotropic two-phase materials. However, the sole microstructural information included in these bounds is the volume fractions (one-point probability functions) of the respective constituents. Three-point bounds for the effective permittivity were introduced by Beran [23], and these bounds were later simplified independently by Torquato [24] and Milton [25] as a function of the volume fraction c_q and a microstructural parameter ζ_q of each material phase q . Beran & Molneux [26], McCoy [27] and Milton & Phan-Thien [28] derived three-point bounds for the effective shear and bulk moduli incorporating c_q , ζ_q and an additional microstructural parameter η_q . These microstructural parameters ζ_q and η_q depend on three-dimensional integrals involving one-, two- and three-point probability functions. While additional theories have been introduced incorporating nonlinear material response [29] and imperfect interface behaviour [30], demonstration of these theories has been severely restricted. Strong microstructural assumptions are an impediment to accurately computing ζ_q and η_q for complex microstructures. Therefore, application of third-order models has been primarily directed to systems of spheres.

Many have studied systems of overlapping spheres [31–34], where the probability functions can be described by a simple exponential decay function. Numerical methods have also been proposed for computing the n -point probability functions directly from microstructures [32,35]. However, application of these methods has been limited to computationally generated morphologies of overlapping spheres [36] or imaging approaches of real systems like sandstone,

which closely resemble the overlapping sphere model [37]. More complex configurations of impenetrable spheres were considered by Torquato and co-workers [38–41], where the microstructural parameters ζ_q and η_q were computed using a statistical mechanics or a single-body operator concept. These methods unfortunately bypassed the computation of the probability functions and have thus proved inaccurate. Despite years of progress in computing these microstructural parameters, direct computation of the statistical functions from three-dimensional microstructural domains with resolution required in third-order models has been elusive until the recent work of Gillman & Matouš [42].

The adaptive numerical method introduced in [42] to compute statistical information directly from three-dimensional microstructures is designed to extend beyond systems of spheres and allows for investigation of an inclusion shape effect. In this work, we extend the computational framework presented in [42] to the microstructural parameter η_q , and a unique study is conducted on the effective thermal conductivity and elastic constants for highly filled isotropic systems of crystalline inclusions (Platonic solids). First, we present an overview of the mathematical theory of third-order statistical micromechanics. Next, we describe and rigorously verify the adaptive numerical methods for computing ζ_q and η_q in third-order models. For the first time, novel predictions of the effective thermo-mechanical properties for isotropic systems of Platonic solids are obtained.

2. Mathematical theory

In this section, a brief summary of higher order statistical micromechanics is presented for computing the effective thermal conductivity and elastic constants of statistically isotropic microstructures.

(a) n -point probability functions

In this work, n -point probability functions are used to describe the morphology of a heterogeneous material. First, a phase indicator function of material phase q at a position $\mathbf{x} \in \mathbb{R}$ in a material sample α of an ensemble space \mathcal{E} is given by

$$\chi_q(\mathbf{x}; \alpha) = \begin{cases} 1 & \text{if } \mathbf{x} \text{ in phase } q \\ 0 & \text{otherwise.} \end{cases} \quad (2.1)$$

The ensemble average (indicated by overbar) of this indicator function is defined as

$$\overline{\chi_q(\mathbf{x})} = \int_{\mathcal{E}} \chi_q(\mathbf{x}; \alpha) p(\alpha) d\alpha, \quad (2.2)$$

where $p(\alpha)$ is the probability density function of α in \mathcal{E} . Using this definition, the n -point probability function, $S_{qs\dots t}(\mathbf{x}_1, \mathbf{x}_2, \dots, \mathbf{x}_n)$, reads

$$S_{qs\dots t}(\mathbf{x}_1, \mathbf{x}_2, \dots, \mathbf{x}_n) = \overline{\chi_q(\mathbf{x}_1)\chi_s(\mathbf{x}_2)\cdots\chi_t(\mathbf{x}_n)}, \quad (2.3)$$

and represents the probability of phases q, s, \dots, t existing at points $\mathbf{x}_1, \mathbf{x}_2, \dots, \mathbf{x}_n$, simultaneously.

In this work, materials containing statistically homogeneous (translationally invariant) and isotropic (rotationally invariant) phases are considered. For statistically homogeneous systems, it is useful to define volume averages. When assuming ergodicity of homogeneous systems, ensemble averaging corresponds to volume averaging in the infinite volume limit

$$S_{qs\dots t}(\mathbf{x}_1, \mathbf{x}_2, \dots, \mathbf{x}_n) = \lim_{\Omega \rightarrow \infty} \frac{1}{\Omega} \int_{\Omega} \chi_q(\mathbf{x}_1 - \mathbf{l})\chi_s(\mathbf{x}_2 - \mathbf{l})\cdots\chi_t(\mathbf{x}_n - \mathbf{l}) d\Omega, \quad (2.4)$$

where \mathbf{l} is a translation vector, and Ω is the volume of the domain. For ergodic, homogeneous and isotropic systems, the one-, two- and three-point probability function reduce to $S_q(\mathbf{x}_1) = c_q$, $S_{qs}(\mathbf{x}_1, \mathbf{x}_2) = S_{qs}(r_1 = |\mathbf{x}_2 - \mathbf{x}_1|)$ and $S_{qst}(\mathbf{x}_1, \mathbf{x}_2, \mathbf{x}_3) = S_{qst}(r_1 = |\mathbf{x}_2 - \mathbf{x}_1|, r_2 = |\mathbf{x}_3 - \mathbf{x}_1|, \theta)$, where θ is the angle between the vectors $\mathbf{x}_2 - \mathbf{x}_1$ and $\mathbf{x}_3 - \mathbf{x}_1$. Moreover, long range order is also absent for

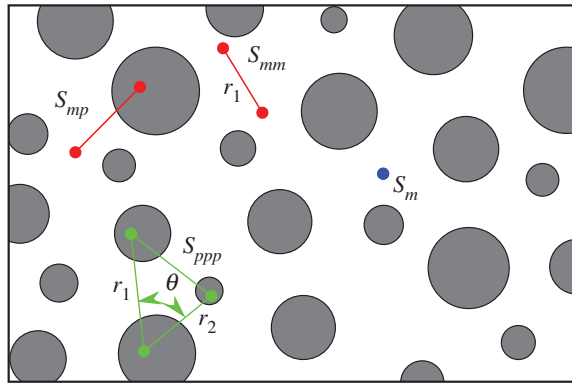


Figure 1. Illustration of n -point probability function sampling with $n - 1$ simplices. (Online version in colour.)

randomly configured microstructures, and the following limits hold for the two-point probability functions

$$S_{qs}(x_2 - x_1) \rightarrow \begin{cases} c_q \delta_{qs} & \text{as } x_2 - x_1 \rightarrow \mathbf{0} \\ c_q c_s & \text{as } x_2 - x_1 \rightarrow \infty, \end{cases} \quad (2.5)$$

and three-point probability functions

$$S_{qst}(x_2 - x_1, x_3 - x_1) \rightarrow \begin{cases} c_q \delta_{ts} & \text{as } x_2 - x_1 \rightarrow \mathbf{0}, x_3 - x_1 \rightarrow \mathbf{0} \\ S_{qs}(x_2 - x_1) \delta_{ts} & \text{as } x_2 - x_3 \rightarrow \mathbf{0} \\ c_q c_s c_t & \text{as } x_2 - x_1 \rightarrow \infty, x_2 - x_3 \rightarrow \infty. \end{cases} \quad (2.6)$$

More details on statistical characterization of heterogeneous materials can be found in a book by Torquato [3].

Analytical expressions of the n -point probability functions do not generally exist for random morphologies. Therefore, Monte Carlo (MC)-based statistical sampling algorithms are often used. When computing function values of a n -point probability function, many random samples or throws are considered and averaged. The accuracy of MC methods is $\mathcal{O}(1/\sqrt{N_r})$. We use high-performance computing to speed up the analysis employing our in-house software package *Stat3D*. The N_r random samples are decomposed on $\mathcal{O}(10^3)$ computing cores. A random sample, N_r , consists of a random translation (described by three position values) and random rotation (described by three angles) of a $(n-1)$ -simplex within the three-dimensional microstructure as illustrated in figure 1. For example, computing a function value of the isotropic three-point probability function $S_{qst}(r_1, r_2, \theta)$ requires random placement of a triangle (a two-simplex) described by two side lengths, r_1 and r_2 , and the angle between the sides θ . In a similar manner, the two-point probability function $S_{qs}(r_1)$ requires random samples of a line segment (one-simplex) with length r_1 .

Figure 2 shows selected planes of θ for the isotropic three-point probability function, $S_{ppp}(r_1, r_2, \theta)$, for a system of impenetrable (non-overlapping) spheres considered by Gillman & Matouš [42]. Note that this pack was generated using a packing algorithm [43] based on the Lubachevsky–Stillinger method [44,45]. Others have computed one-, two- and three-point probability functions for systems of spheres for the purpose of quantifying the configuration [46,47]. However, computing these complex functions for the entire function domain, Ω , with the fidelity required by third-order statistical micromechanics models presented in §2b has not been previously accomplished. Therefore, we introduce the adaptive interpolation strategy described in §3 to overcome these difficulties. See [42] for brief information on the adaptive interpolation scheme.

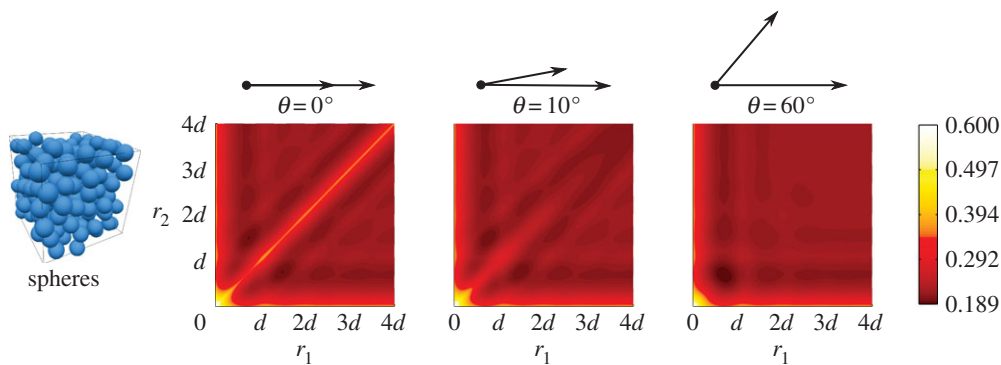


Figure 2. Three-point probability function, $S_{ppp}(r_1, r_2, \theta)$, for the isotropic system of spheres with $c_p = 0.6$. (Online version in colour.)

(b) Third-order models of effective material behaviour

For completeness of presentation, this section summarizes the statistical micromechanics theories. Books by Milton [48] and Torquato [3] present the detailed mathematical theory for determining effective material properties.

(i) Thermal conductivity

Regarding effective thermal properties, the steady-state heat conduction problem is considered. At the local scale, the conservation of energy is

$$\nabla \cdot \mathbf{q}(x) = 0 \quad \text{in } \Omega, \quad (2.7)$$

where $\mathbf{q}(x)$ denotes the heat flux at a spatial point $x \in \mathbb{R}$ of the domain Ω . The heat flux is related to the temperature field, $T(x)$, assuming Fourier's Law

$$\mathbf{q}(x) = \kappa(x) \cdot \mathbf{Q}(x), \quad (2.8)$$

where $\kappa(x)$ is the second-order thermal conductivity tensor and $\mathbf{Q}(x) = -\nabla T(x)$. The local thermal conductivity for a two-phase particulate composite is defined as

$$\kappa(x) = \kappa_m \chi_m(x) + \kappa_p \chi_p(x) = \kappa_m(1 - \chi_p(x)) + \kappa_p \chi_p(x), \quad (2.9)$$

where the subscripts p and m denote the particle and matrix phases, respectively.

Using variational principles, Beran [23] derived third-order bounds for the effective thermal conductivity, $\kappa^L \leq \kappa_e \leq \kappa^U$, of homogeneous and isotropic heterogeneous materials. The superscripts L and U denote the lower and upper bounds, respectively. The bounds were later simplified by Milton [25] and Torquato [24] for two-phase materials assuming isotropic material behaviour and are given as

$$\left. \begin{aligned} \kappa^L &= c_p \kappa_p + c_m \kappa_m - \frac{c_m c_p (\kappa_p - \kappa_m)^2}{c_m \kappa_p + c_p \kappa_m + 2(\zeta_p / \kappa_p + \zeta_m / \kappa_m)^{-1}} \\ \kappa^U &= c_p \kappa_p + c_m \kappa_m - \frac{c_m c_p (\kappa_p - \kappa_m)^2}{c_m \kappa_p + c_p \kappa_m + 2(\zeta_p \kappa_p + \zeta_m \kappa_m)}. \end{aligned} \right\} \quad (2.10)$$

and

These bounds are a function of the volume fraction, c_q , the local conductivity, κ_q , and the microstructural parameter, ζ_q , of the particle ($q = p$) and matrix ($q = m$) material phases. The

microstructural parameter, ζ_q is defined as

$$\zeta_q = \frac{9}{2c_p c_m} \int_0^\infty \int_0^\infty \int_{-1}^1 \frac{3 \cos^2 \theta - 1}{2r_1 r_2} \tilde{S}_{qqq}(r_1, r_2, \theta) d(\cos \theta) dr_1 dr_2, \quad (2.11)$$

where

$$\tilde{S}_{qqq}(r_1, r_2, \theta) = \frac{S_{qqq}(r_1, r_2, \theta) - S_{qq}(r_1)S_{qq}(r_2)}{c_q}. \quad (2.12)$$

For isotropic two-phase systems, Torquato [49] derived a three-point approximation (TPA) that has shown good agreement with simulations [50] for microstructures containing dispersions of particles without large clustering. This estimate is given as

$$\frac{\kappa_e}{\kappa_m} = \frac{1 + 2c_p \kappa_{pm} - 2c_m \zeta_p \kappa_{pm}^2}{1 - c_p \kappa_{pm} - 2c_m \zeta_p \kappa_{pm}^2}, \quad (2.13)$$

where

$$\kappa_{pm} = \frac{\kappa_p - \kappa_m}{\kappa_p + 2\kappa_m}. \quad (2.14)$$

(ii) Elastic constants

When considering the effective mechanical response, the conservation of linear momentum neglecting inertia and body forces reads

$$\nabla \cdot \boldsymbol{\sigma}(\mathbf{x}) = \mathbf{0} \quad \text{in } \Omega, \quad (2.15)$$

where $\boldsymbol{\sigma}(\mathbf{x})$ is the symmetric second-order stress tensor at a point $\mathbf{x} \in \mathbb{R}$. The state of stress is related to the infinitesimal strain tensor, $\boldsymbol{\varepsilon}(\mathbf{x}) = \frac{1}{2}(\nabla \mathbf{u}(\mathbf{x}) + \nabla \mathbf{u}(\mathbf{x})^T)$, assuming Hooke's Law,

$$\boldsymbol{\sigma}(\mathbf{x}) = \mathbf{L}(\mathbf{x}) : \boldsymbol{\varepsilon}(\mathbf{x}). \quad (2.16)$$

Here, $\mathbf{u}(\mathbf{x})$ is the local displacement field, and $\mathbf{L}(\mathbf{x})$ is the local elasticity tensor given as

$$\mathbf{L}(\mathbf{x}) = \mathbf{L}_m \chi_m(\mathbf{x}) + \mathbf{L}_p \chi_p(\mathbf{x}) = \mathbf{L}_m(1 - \chi_p(\mathbf{x})) + \mathbf{L}_p \chi_p(\mathbf{x}). \quad (2.17)$$

Note that for an isotropic material, $\mathbf{L}_q = 3K_q \mathbf{A}_h + 2G_q \mathbf{A}_s$, where K_q and G_q are the bulk and shear moduli of material phase q , and the hydrostatic and shear projection tensors are defined as $\mathbf{A}_h = \frac{1}{3} \mathbf{1} \otimes \mathbf{1}$ and $\mathbf{A}_s = \mathbf{I} - \frac{1}{3} \mathbf{1} \otimes \mathbf{1}$, respectively. $\mathbf{1}$ and \mathbf{I} are the second and symmetric fourth-order identity tensors.

Using variational principles, third-order bounds of the effective bulk ($K^L \leq K_e \leq K^U$) and shear moduli ($G^L \leq G_e \leq G^U$) have been derived by Beran & Molyneux [26], McCoy [27], and were later simplified and improved upon by Milton [25], Milton & Phan-Thien [28] and Gibiansky & Torquato [51]. The bounds of the effective moduli considered in this work are given in Milton & Phan-Thien [28] as

$$\left. \begin{aligned} K^L &= c_p K_p + c_m K_m - \frac{c_m c_p (K_p - K_m)^2}{c_m K_p + c_p K_m + (4/3)(\zeta_p/G_p + \zeta_m/G_m)^{-1}} \\ K^U &= c_p K_p + c_m K_m - \frac{c_m c_p (K_p - K_m)^2}{c_m K_p + c_p K_m + (4/3)(\zeta_p G_p + \zeta_m G_m)}, \end{aligned} \right\} \quad (2.18)$$

and

$$\left. \begin{aligned} G^L &= c_p G_p + c_m G_m - \frac{c_m c_p (G_p - G_m)^2}{c_m G_p + c_p G_m + \mathcal{E}_L} \\ G^U &= c_p G_p + c_m G_m - \frac{c_m c_p (G_p - G_m)^2}{c_m G_p + c_p G_m + \mathcal{E}_U}, \end{aligned} \right\} \quad (2.19)$$

where \mathcal{E}_L and \mathcal{E}_U are presented in appendix A. The bounds are functions of $K_m, K_p, G_m, G_p, c_m, c_p, \zeta_m, \zeta_p, \eta_m$ and η_p . Note that in addition to the microstructural parameter ζ_q that also appeared

in the bounds of the effective thermal conductivity, the bounds of the shear modulus are functions of an additional microstructural parameter η_q . This parameter is defined as

$$\eta_q = \frac{5\zeta_q}{21} + \frac{150}{7c_p c_m} \int_0^\infty \int_0^\infty \int_{-1}^1 \frac{P_4(\cos\theta)}{r_1 r_2} \tilde{S}_{qqq} d(\cos\theta) dr_1 dr_2. \quad (2.20)$$

Similar to the TPA presented for the effective thermal conductivity (see equation (2.13)), Torquato [52,53] has more recently derived a TPA for the effective bulk and shear modulus (see appendix A).

3. Adaptive interpolation/integration method for computing microstructural parameters

The integrals presented in equations (2.11) and (2.20) for computing the microstructural parameters ζ_q and η_q involve the interaction of the one-, two- and three-point probability functions. Moreover, the statistics are multiplied by the term $1/(r_1 r_2)$ in the integral kernel. When the values for r_1 and r_2 are small, the error in the statistics values can be substantially amplified. These interactions, especially for systems with complex statistics functions (figure 2) have prevented the accurate evaluation of ζ_q and η_q for particulate microstructures until recent work of Gillman & Matouš [42]. In this section, we expand on the numerical methods introduced in [42] for constructing an adaptive interpolant of $\tilde{S}_{qqq}(r_1, r_2, \theta)$ and numerically integrating equations (2.11) and (2.20).

Others [46,54] have attempted an MC sampling strategy to compute probability functions, but on regular structured grids. An adaptive triangulation technique is used to overcome inefficiencies of structured grids. To simply explain our adaptive scheme, an illustration is shown for a two-dimensional product peak function introduced by Genz [55] in figure 3. This function is typical for testing multi-dimensional numerical integration schemes and is defined as

$$f_G(x_1, x_2) = \frac{1}{(a_1^{-2} + (x_1 - w_1)^2)(a_2^{-2} + (x_2 - w_2)^2)}, \quad (3.1)$$

where the constants are set to $a_1 = 5$, $a_2 = 10$, $w_1 = 0.25$ and $w_2 = 0.4$ for this example.

In order to capture the important features of this function, a Delaunay triangulation is iteratively constructed with C^0 continuity using the CGAL library [56,57]. The triangulation is denoted as \mathcal{T} . Initially, a regular discretization is constructed (figure 3c). This triangulation and associated function values, $f(x_1, x_2, \dots, x_n)$, define the initial interpolant $\mathcal{T}_{l=0}$ (l is the adaptive level). For a given iteration, a bisection method is used to refine the triangulation based on the local error of the interpolant. For all triangles/tetrahedrons in a given iteration of the interpolant \mathcal{T}_l , the local accuracy is evaluated at each edge midpoint by introducing an error indicator function, $\tilde{\varepsilon} = |f(x_1, x_2, \dots, x_n) - \mathcal{T}_l(x_1, x_2, \dots, x_n)|$. If an edge midpoint error is $\tilde{\varepsilon} > \text{tol}$, where tol is a tolerance, each edge of the triangle/tetrahedron is bisected and added to \mathcal{T}_{l+1} . If all midpoints in a tetrahedron satisfy $\tilde{\varepsilon} \leq \text{tol}$, the triangle/tetrahedron is added to \mathcal{T}_{l+1} unchanged. An illustration of this bisection method is shown in figure 3b, where the line segment along $x_1 = 0.5$ is considered. The solid black line is the smooth function, $f_G(x_1 = 0.5, x_2)$, and the dashed black line is the initial interpolant, $\mathcal{T}_{l=0}(x_1 = 0.5, x_2)$. Midpoints that satisfy $\tilde{\varepsilon} \leq \text{tol}$ are marked with circles, and those that do not are marked with x's. All triangles with a midpoint marked with an x are bisected. This iterative process is repeated until all grid points satisfy the $\tilde{\varepsilon} \leq \text{tol}$.

In this work, the adaptive triangulation technique is used to create an interpolant of $\tilde{S}_{qqq}(r_1, r_2, \theta)$ as defined in equation (2.12). The initial regular tetrahedral grid is constructed for the domain $[r_1 = 0, r_1 = r^\infty] \times [r_2 = 0, r_2 = r_1] \times [\theta = 0, \theta = \pi]$ (note that this is half of the integration domain since the function is symmetric about the axis $r_1 = r_2$). This triangulation and associated function values, $\tilde{S}_{qqq}(r_1, r_2, \theta)$, define the interpolant \mathcal{T} . After a convergence study, it was determined that setting $\text{tol} = \frac{1}{200} \max\{\tilde{S}_{qqq}(r_1, r_2, \theta)\}$ results in low numerical error for all computations presented in this work. Using the interpolant \mathcal{T} , the microstructural parameters,

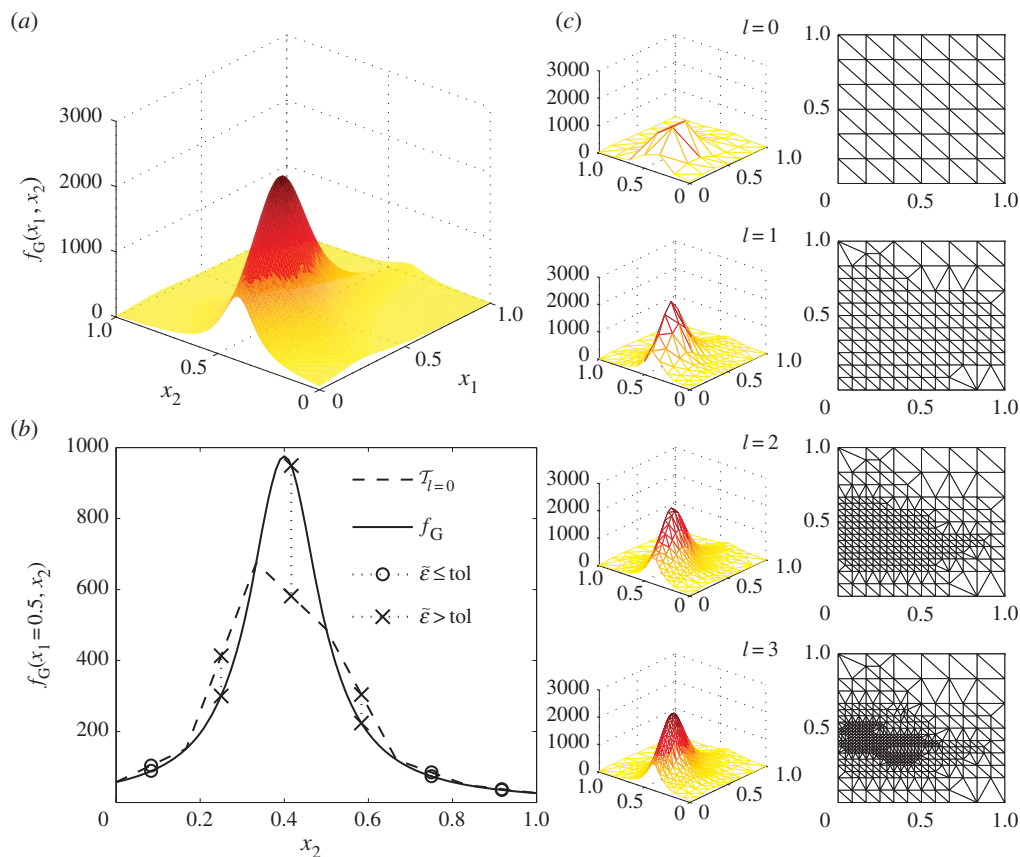


Figure 3. (a–c) Illustrations of adaptive interpolation of a function by Delaunay triangulation. (Online version in colour.)

ζ_q and η_q in equations (2.11) and (2.20), are computed via simplex integration. MC integration of each tetrahedron is performed [58], and a convergence study determined that using $N_{\text{int}} = 1000$ random integration points per tetrahedron is sufficient for all particulate systems considered. Given that there are $\mathcal{O}(10^7)$ tetrahedrons in a typical interpolant, $\mathcal{O}(10^{10})$ integration points are required to evaluate the integrals in equations (2.11) and (2.20). To perform these challenging computations, we use 500–7200 computing cores on Los Alamos National Laboratories’ Mustang and Notre Dame’s C-SWARM clusters.

4. Numerical results

Using the methods described in the prior sections, bounds and estimates of the effective thermal conductivity and elastic constants were computed with the well-resolved (WR) statistical description. First, verification studies were conducted on commonly studied microstructures of overlapping and impenetrable spheres. After verification of the methods, results are presented for statically isotropic systems of Platonic solids. Note that throughout this section, we denote our results with WR due to use of WR statistics.

(a) Verification

In order to assess the accuracy of our numerical method, a verification study was conducted. The interpolation/integration scheme is verified using the analytical form of the overlapping sphere model. Then, the methods are used with MC sampling for systems of impenetrable spheres. The

Table 1. Verification of the adaptive interpolation and integration method for computing equations (2.11) and (2.20) assuming penetrable sphere model. Comparison is made between results of this work (ζ_m, η_m) and results in [34] ($\zeta_m^{R1}, \eta_m^{R1}$). Results for ζ_m were published in [42].

c_p	ζ_m	ζ_m^{R1}	ε_{PS}^ζ (%)	η_m	η_m^{R1}	ε_{PS}^η (%)
0.2	0.5187	0.5174	0.24	0.4178	0.4163	0.35
0.4	0.6571	0.6489	1.26	0.5579	0.5604	0.44
0.6	0.7743	0.7702	0.54	0.6987	0.7050	0.89

resulting predictions of the effective thermal conductivity and elastic constants are compared to simulation data.

(i) Penetrable sphere model

For the purpose of verification, microstructures composed of overlapping spheres are studied. This is one of the few systems, where the n -point probability functions can be defined analytically. The probability function for the matrix phase is defined as

$$S_{m\dots m}(x_1, x_2, \dots, x_n) = \exp(-\rho V_n), \quad (4.1)$$

where ρ is the number density of spheres and V_n is the union volume of n spheres with diameter d .

Using this analytical expression for the n -point probability function, an interpolant is created for $\tilde{S}_{qqq}(r_1, r_1, \theta)$ (equation (2.12)) with $\text{tol} = \frac{1}{200} \max\{\tilde{S}_{qqq}(r_1, r_2, \theta)\}$ and $r^\infty = 6d$. Following construction of this interpolant, MC integration is used to compute the integrals appearing in equations (2.11) and (2.20). The resulting values of ζ_m and η_m are presented in table 1. Note that results for ζ_m (or ζ_p) were first presented in [42] and are provided here for completeness. In order to assess the accuracy of these methods, the values computed in this work are compared to the most accurate result presented in the literature [34]. Error measures introduced to quantify the accuracy of the microstructural parameters are defined as $\varepsilon_{PS}^\zeta = |\zeta_m - \zeta_m^{R1}| / \zeta_m^{R1} \times 100[\%]$ and $\varepsilon_{PS}^\eta = |\eta_m - \eta_m^{R1}| / \eta_m^{R1} \times 100[\%]$. Note that all results computed with the adaptive methods have errors below 2% (table 1). Thus, the adaptive interpolation and integration methods are considered verified for the range of volume fractions considered in this work.

(ii) Random systems of impenetrable spheres

Following verification of the penetrable sphere model, systems of impenetrable (non-overlapping) monodisperse spheres are considered. Such systems have been studied extensively by Torquato and co-workers [38–40]. However, despite significant progress, computing the microstructural parameters ζ_q and η_q for three-dimensional systems directly has been unachievable (due to the complexity of the n -point probability functions) until the recent work on thermal conductivity of Gillman & Matouš [42].

The same monodisperse sphere systems presented in [42] for verification of the effective thermal conductivity are considered for verification of the third-order estimates of the effective bulk and shear moduli. These systems were generated using a packing algorithm [43] based on the Lubachevsky–Stillinger method [44,45]. Cubic domains consisting of $\mathcal{O}(10^4)$ particles with diameter d were generated, and a high expansion rate was prescribed to ensure statistical isotropy. After a convergence study, it was determined that $r^\infty = 12d$ is required to compute ζ_p and η_p with acceptable accuracy. Furthermore, the convergence study uncovered that it is necessary to use $N_r = 10^7$ random samples for each n -point probability function evaluation in equation (2.12) to satisfy the tolerance tol . The computed microstructural parameters ζ_p and η_p are presented in table 2. Comparison is made to approximations given in [40,59]. The improvement of ζ_p from the result presented in [40], denoted as ζ_p^{R2} , is quantified by introducing an error metric $\varepsilon_{IS}^\zeta = |\zeta_p - \zeta_p^{R2}| / \zeta_p^{R2} \times 100[\%]$. Reasonable agreement for ζ_p is shown for lower volume fractions,

Table 2. Comparison of ζ_p and η_p for random impenetrable monodisperse sphere systems. Comparison is made between results presented in this work (ζ_p, η_p) and results in [40] (ζ_p^{R2}) and [59] (η_p^{R3}). Results for ζ_p were published in [42].

c_p	ζ_p	ζ_p^{R2}	ε_{IS}^ζ (%)	η_p	η_p^{R3}	ε_{IS}^η (%)
0.2	0.0442	0.0409	8.17	0.084	0.097	13.5
0.4	0.0883	0.0765	15.37	0.192	0.193	0.3
0.5	0.1114	0.0938	18.78	0.252	0.241	4.4
0.6	0.1967	0.134	46.78	0.342	0.290	18.0

Table 3. Comparison of third-order lower bounds K_e^L and G_e^L for random impenetrable monodisperse sphere systems with infinite material contrast. Comparison is made between WR bounds and bounds computed with data from [40,59] (R2,R3, see table 2).

c_p	K_e^{L-WR}/K_m	K_e^{L-R2}/K_m	ε_{IS}^K (%)	G_e^{L-WR}/G_m	$G_e^{L-R2,R3}/G_m$	ε_{IS}^G (%)
0.2	1.46	1.46	0.05	1.53	1.53	0.14
0.4	2.25	2.24	0.32	2.49	2.49	0.15
0.5	2.90	2.88	0.60	3.31	3.29	0.64
0.6	3.99	3.89	2.78	4.70	4.54	3.54

but significant improvement has been achieved for higher volume fractions. For the parameter η_p , the results are compared to the work of Torquato *et al.* [59]. The differences from the results in [59] are quantified by the following metric $\varepsilon_{IS}^\eta = |\eta_p - \eta_p^{R3}|/\eta_p^{R3} \times 100[\%]$. Note that the metric ε_{IS}^η is non-monotonic with respect to c_p . However, this is not unexpected given the simple inaccurate relation, $\eta_p = 0.4827c_p$, derived in [59], as η_p is only first-order accurate with respect to c_p .

The computed microstructural parameters, ζ_p and η_p , are then used within the third-order statistical micromechanics theories for the effective bulk and shear moduli as described in §2b(ii). We use our in-house software package *Prop3D* to compute all thermo-mechanical properties. In the remainder of this work, an infinite contrast ratio between particle and matrix phases is considered ($K_p/K_m = \infty$, $G_p/G_m = \infty$ and $\nu_m = 0.25$). The WR three-point lower bounds K_e^{L-WR} and G_e^{L-WR} (see equations (2.18) and (2.19)) are presented in table 3 and compared to the bounds using ζ_p^{R2} and η_p^{R3} from [40,59]. Differences in K_e^L and G_e^L are quantified as $\varepsilon_{IS}^K = |K_e^{L-WR} - K_e^{L-R2}|/K_e^{L-R2} \times 100[\%]$ and $\varepsilon_{IS}^G = |G_e^{L-WR} - G_e^{L-R2,R3}|/G_e^{L-R2,R3} \times 100[\%]$. As expected, the differences are small for lower particle volume fractions, as marginal improvement was seen for ζ_p and η_p (table 2). However, for $c_p = 0.6$, where improvements in ζ_p and η_p were 46.8% and 18.0%, respectively, the lower bounds of K_e and G_e are improved by 2.78% and 3.54%.

In figure 4, we show results for the well-resolved three-point approximation (TPA-WR, solid line with circles) of K_e and G_e (see equations (A 2) and (A 5)). These results are compared to FEM data from Segurado & Llorca [60] (filled circles), the TPA using Torquato's approximations [40,59] (TPA, dash-dotted line) and the widely used Hashin-Shtrikman bound (HS, dashed line). Note that the HS bounds (presented in appendix B) are unable to capture details of the morphology other than the volume fraction, c_p , and is the least accurate prediction. When comparing TPA-WR to Torquato's TPA, the largest improvement in the estimate of K_e and G_e is seen for higher volume fractions. For the volume fraction $c_p = 0.6$, the estimates of the bulk modulus and shear modulus have been improved by 5.25% and 6.4%, respectively. Note that the improvement in the elastic constants is less pronounced than those of the effective thermal conductivity [42] (17.4% improvement in κ_e achieved for $c_p = 0.6$). This smaller improvement shows that the third-order estimates for the elastic constants are less sensitive to the morphology. When comparing the TPA-WR to finite-element method (FEM) data in [60] (filled black circles), all finite-element method (FEM) data points are within 4.3% of the TPA-WR for the bulk modulus (K_e) and within

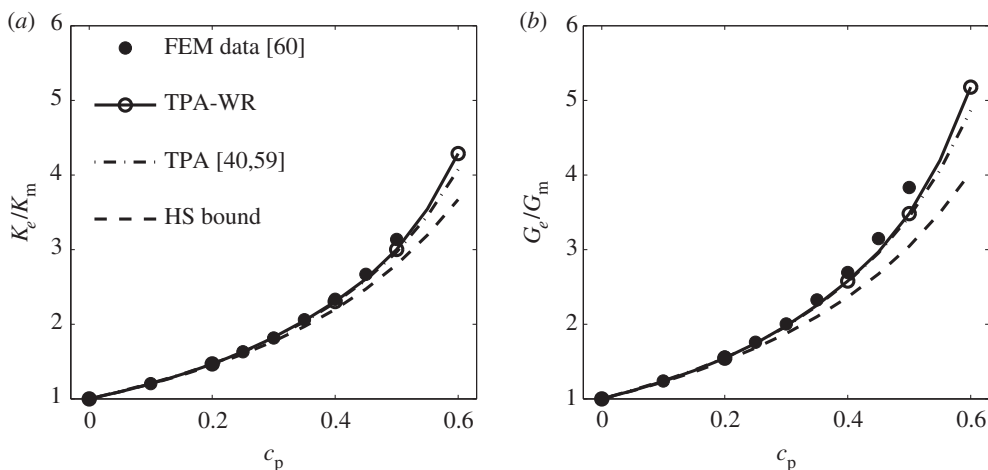


Figure 4. TPA of (a) bulk modulus and (b) shear modulus for isotropic systems of spheres with infinite contrast ratio.

9% of the TPA-WR for the shear modulus (G_e). We point out that FEM data are not error free. Therefore, small differences between our statistical micromechanics and FEM results [60] for K_e and G_e must be interpreted more qualitatively. It is also important to note that the FEM data presented in [60] is only reported for particle volume fractions up to $c_p = 0.5$. Direct numerical modelling methods like FEM can become challenging for highly filled systems due to numerical issues, especially for high material contrast. However, the computational complexity of higher order statistical micromechanics presented in this work does not increase for highly filled packs.

(b) Random systems of Platonic solids

As mentioned in the Introduction, predicting the effective material behaviour of particulate materials by third-order statistical micromechanics has proved elusive due to numerical difficulties. Therefore, in this section, we elucidate the importance of our WR computations with the novel application of these theories to packs of monodisperse Platonic solids. For the first time, the statistical micromechanics is applied to crystalline packs (Platonic solids) with fidelity and resolution needed for meaningful thermo-mechanical engineering analysis.

(i) Generation of microstructures

To study the effect of inclusion shape on the effective material properties, the packing code *Rocpack* [61–63] is used to generate statistically isotropic systems of Platonic solids. The algorithm is a hybrid of the Lubachevsky–Stillinger [44] and Adaptive Shrinking Cell [64,65] packing algorithms, where infinitesimal particles are randomly distributed within a volume and allowed to grow until a desired volume fraction is reached. Collisions are handled to prevent particle intersection and maintain statistical isotropy. In this work, packs with volume fractions of $c_p = 0.2, 0.4, 0.5$ and 0.6 containing $N_p = 10\,313, 20\,626, 25\,783$ and $30\,940$ particles, respectively, are packed in a unit cubic volume. This corresponds to a side length of approximately $30d$, where d is the equivalent sphere diameter (diameter computed from volume of a particle assuming spherical shape).

Geometric quantities associated with the Platonic solids are summarized in table 4. The number of faces (N_F), vertices (N_V) and edges (N_E) are presented along with the dihedral angle (α), inradius (R_{in}), midradius (R_{mid}) and circumradius (R_{circ}). Note that the inradius (R_{in}) is the radius of an inscribed sphere for the polyhedra, the midradius (R_{mid}) is the radius of a sphere intersecting the midpoints of the edges and the circumradius (R_{circ}) is the radius of a circumscribed sphere. The inradius and dihedral angle (α) increase with the number of faces N_F .

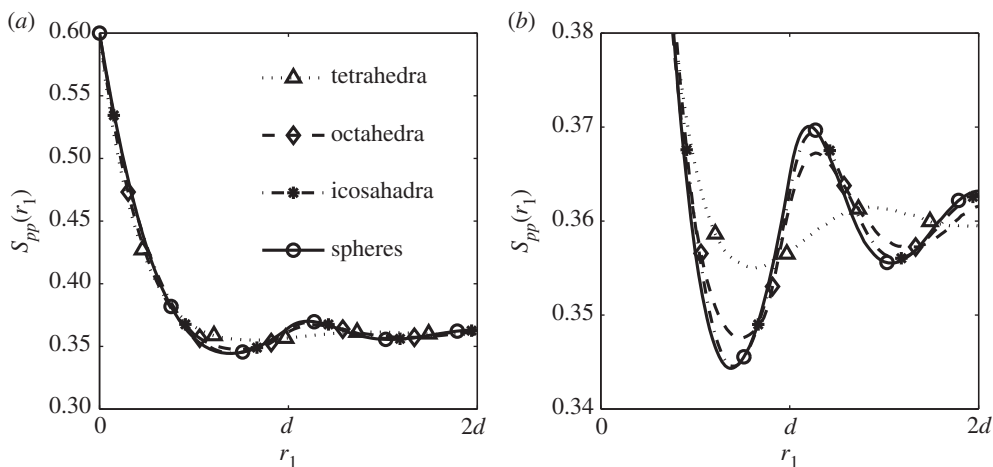


Figure 5. (a, b) Two-point probability function, $S_{pp}(r_1)$, for Platonic solids. Note that d is the equivalent sphere diameter.

Table 4. Geometrical description of each Platonic solid with volume of $4\pi/3$ (equivalent sphere diameter, $d = 2$). The percolation threshold, c_p^{per} for overlapping Platonic solids was determined from numerical simulation by Torquato & Jiao [66].

shape	N_F	N_E	N_V	α	R_{in}	R_{mid}	R_{cir}	c_p^{per}
tetrahedron	4	6	4	70.53°	0.671	1.162	2.013	0.1701
hexahedron	6	12	8	90.0°	0.806	1.140	1.396	0.2443
octahedron	8	12	6	109.47°	0.846	1.036	1.465	0.2514
dodecahedron	12	30	20	116.57°	0.911	1.070	1.146	0.2949
icosahedron	20	30	12	138.19°	0.939	1.006	1.182	0.3030

To aid further analysis, the percolation threshold volume fraction, c_p^{per} , for systems of overlapping shapes from [66] is also presented. Note that c_p^{per} increases with N_F , and the percolation results for overlapping systems assist in explaining the structures and their effect on the effective material response.

(ii) Statistical analysis

After generating the packs of Platonic solids, the systems are statistically characterized. The isotropic two-point probability function $S_{pp}(r)$ for $c_p = 0.6$ packs of tetrahedra, octahedra and icosahedra is shown in figure 5. The functions are compared to the system of spheres considered in §4b(ii). Note that packs with polyhedra that are composed of more faces (N_F) approach the statistical function for a pack of spheres. At the origin ($r = 0$), the slope of the function is steepest for the system of tetrahedra. The three-point probability functions for packs with $c_p = 0.6$ are presented for selected values of θ in figure 6. It can be seen that the system of icosahedra closely resembles the function for spheres (cf. figure 2). Meanwhile, the probability function for the systems of tetrahedra has less complex features. In general, the packs of polyhedra with smaller N_F result in less complex n -point probability functions as compared with ones with more faces. Note that the one-point and two-point probability functions are contained within the three-point probability function (see equations (2.5) and (2.6)). The function $S_{ppp}(r_1, r_2, \theta)$ degenerates to the volume fraction $c_p = 0.6$ at the point $r_1 = r_2 = 0$, and the function degenerates to the two-point probability function along the line $r_1 = r_2$ ($\theta = 0$) and along the planes $r_1 = 0$ and $r_2 = 0$. These degeneracies are used to evaluate the MC sampling error in the statistical functions.

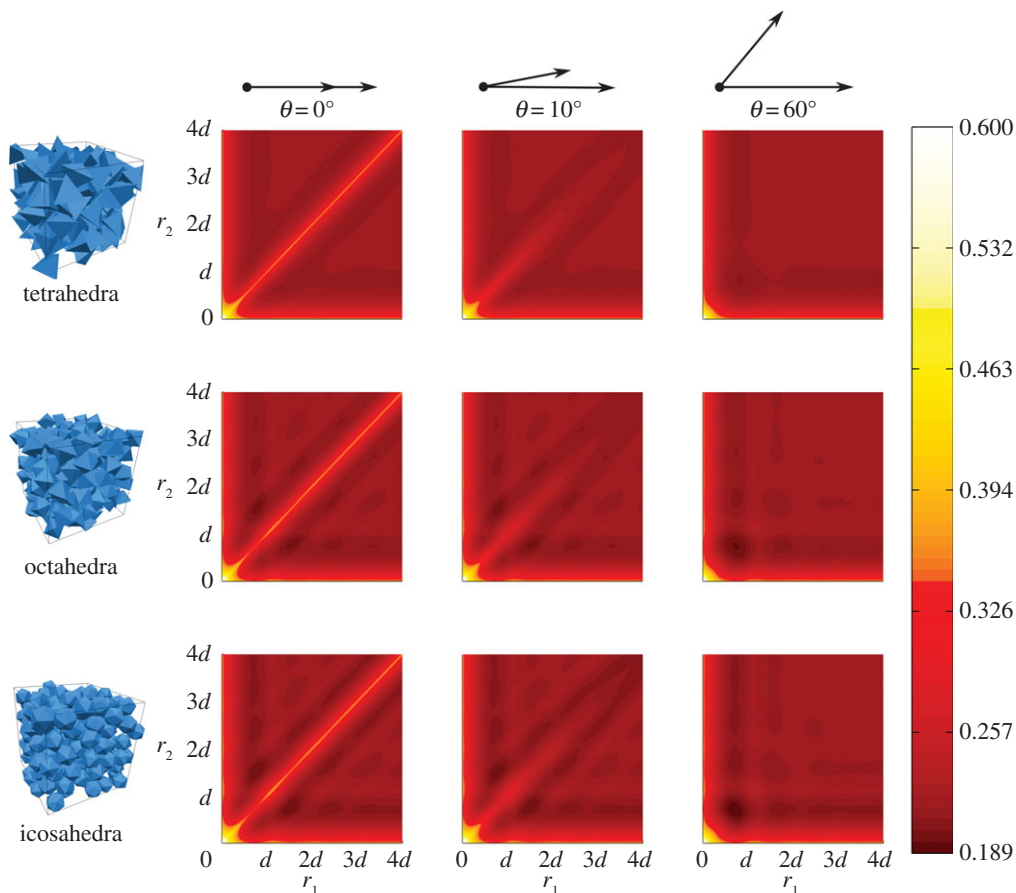


Figure 6. Three-point probability function, $S_{ppp}(r_1, r_2, \theta)$, for isotropic systems of Platonic solids with $c_p = 0.6$. (Online version in colour.)

It is particularly important to understand the error related to the interactions of the probability functions in \tilde{S}_{ppp} (see equation (2.12)). Therefore, two error metrics are constructed to evaluate the sampling error and are defined as $\varepsilon_{S3}^0 = \|\tilde{S}_{ppp}(r_1 = 0, r_2 = 0, \theta)\|_\infty$ and $\varepsilon_{S3}^\infty = |\tilde{S}_{ppp}(r_1 = r^\infty, r_2 = r_1, \theta = \pi)|$. Both error metrics should approach 0 as $N_r \rightarrow \infty$. For all packs with $c_p = 0.2$, both of these error metrics are below 1.3×10^{-4} when the number of random samples is $N_r = 10^7$. For all packs with $c_p = 0.6$, both of these metrics are below 2.7×10^{-4} . These errors are at least $2 \times$ less than the tolerance tol in the adaptive interpolation scheme.

Following the statistical analysis and error quantification, the microstructural parameters ζ_p and η_p are computed. The same numerical parameters reported for the systems of impenetrable spheres ($r^\infty = 12d$ and $N_r = 10^7$) are used. The parameters ζ_p and η_p for all packs of Platonic solids are shown in figure 7*a,b*, respectively. Note that there is a monotonic increase of ζ_p as the number of faces, N_F , decreases. However, the value of η_p does not follow this simple trend.

Considering the local configurations of the shapes aids in understanding the values obtained for η_p . A measure β_{IJ} is introduced to quantify the local arrangement of particles. β_{IJ} , as illustrated in figure 8, is the distance between a particle I and a neighbouring particle J . The minimum distance between particle I and all neighbouring particles is denoted $\beta_I = \min(\beta_{IJ})$. Finally, $\beta = \text{mean}(\beta_I)$ is defined as the average β_I for all particles in a pack. In figure 9*a*, β is presented for each pack and is normalized by the equivalent sphere diameter, d . In order to complement the values of β/d , the distances, β_{12}/d , associated with the various types of contacts between only two

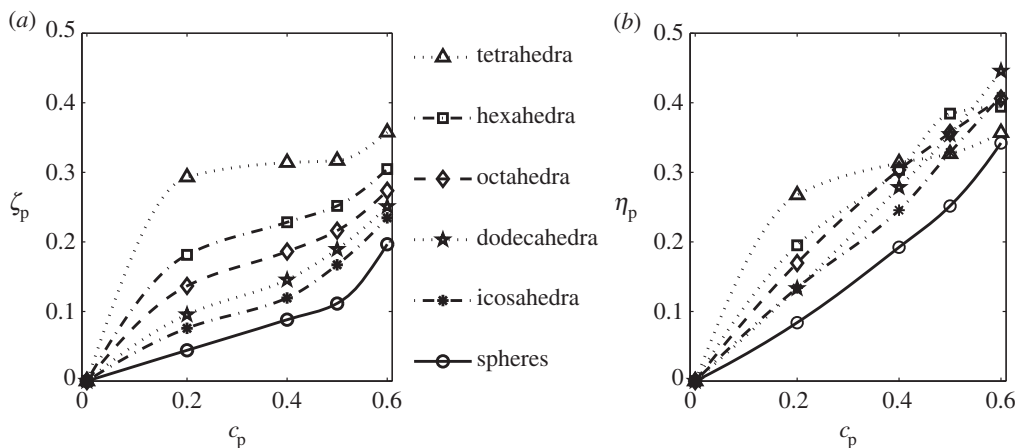


Figure 7. Three-point microstructural parameters (a) ζ_p and (b) η_p for packs of Platonic solids.

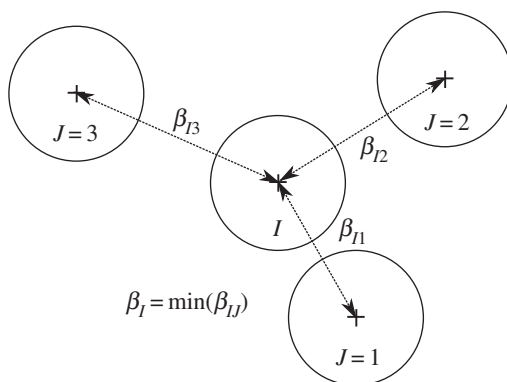


Figure 8. Schematic illustrating the calculation of the distances between particle centres, β_{IJ} . The distance between the nearest neighbour and particle I is denoted β_I .

single Platonic solids are shown in figure 9b. The distances associated with a vertex–vertex (V–V, $\beta_{12} = R_{\text{circ}} + R_{\text{circ}}$), vertex–edge (V–E, $\beta_{12} = R_{\text{circ}} + R_{\text{mid}}$), vertex–face (V–F, $\beta_{12} = R_{\text{mid}} + R_{\text{in}}$), edge–edge (E–E, $\beta_{12} = R_{\text{mid}} + R_{\text{mid}}$), edge–face (E–F, $\beta_{12} = R_{\text{mid}} + R_{\text{in}}$) and face–face (F–F, $\beta_{12} = R_{\text{in}} + R_{\text{in}}$) contact between two particles are presented. The F–F contact represents the lower limit of β/d and corresponds to the inscribed radius, R_{in} (table 4). β_{12}/d less than one signifies particles in close proximity and assembling mostly in a E–F or F–F contact. For illustration, note that two tetrahedrons come in V–V contact at larger distances apart and are closest together with a F–F contact. In figure 9a, β/d is less than one at the smallest volume fractions for the system of tetrahedra. Moreover, when the measure β/d becomes less than one, a significant slope decrease in the function η_p is observed (figure 7b). With tetrahedra for example (dotted line with triangular markers), β/d becomes less than one between $c_p = 0.2 - 0.3$, and a change in slope of η_p is observed near $c_p = 0.2$. A similar change in slope can be also observed for ζ_p as β/d approaches one (figure 7a).

(iii) Third-order estimates of effective material behaviour

With ζ_p and η_p accurately computed, the TPA of the thermal conductivity and bulk and shear moduli are considered. Figure 10 presents the TPA-WR estimates of the thermal conductivity, κ_e ,

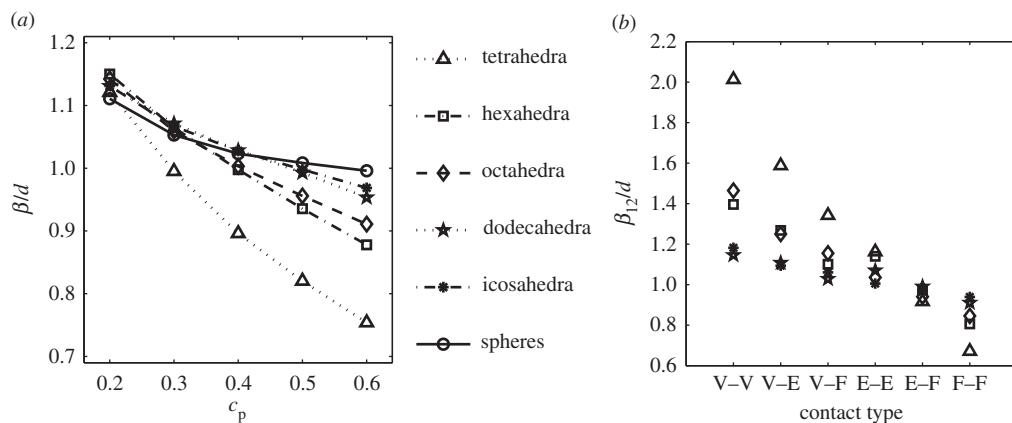


Figure 9. (a) Mean minimum distance of neighbouring particles, β/d , for isotropic systems of Platonic solids as a function of volume fraction, c_p . (b) Distance between only two contacting Platonic solids, β_{12}/d . Contact types are vertex–vertex (V–V), vertex–edge (V–E), vertex–face (V–F), edge–edge (E–E), edge–face (E–F) and face–face (F–F).

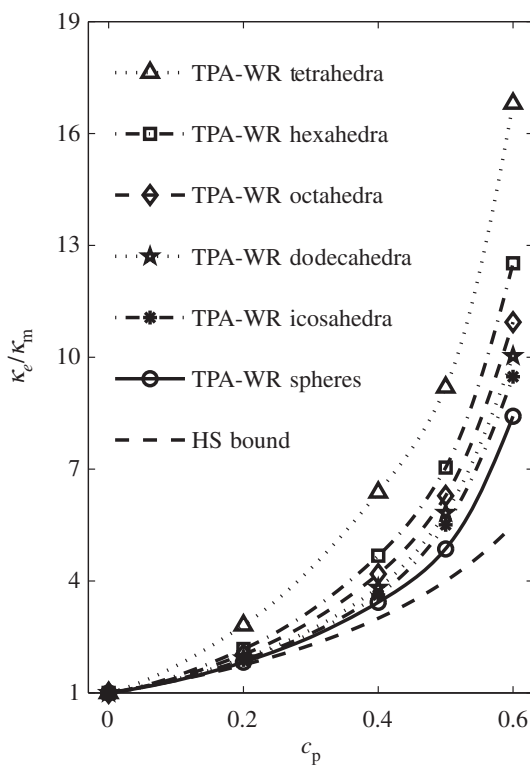


Figure 10. Third-order approximation of thermal conductivity for isotropic systems of Platonic solids with infinite contrast.

using equation (2.13) for an infinite contrast ratio ($\kappa_p/\kappa_m = \infty$). In figure 10, the striking feature is the prominent shape effect in thermal conductivity for different Platonic solids. With tetrahedra for example (dotted line with triangular markers), the normalized effective thermal conductivity (κ_e/κ_m) for $c_p = 0.6$ is 16.81. In comparison to the pack of spheres ($\kappa_e/\kappa_m = 8.42$), the effective thermal conductivity has increased by 1.99 times (99.6% increase). In general, as the number of faces, N_F , decreases, the effective conductivity increases. Moreover, when revisiting the local morphology measure β , tetrahedra came to proximity frequently through F–F contact ($\beta/d < 1$)

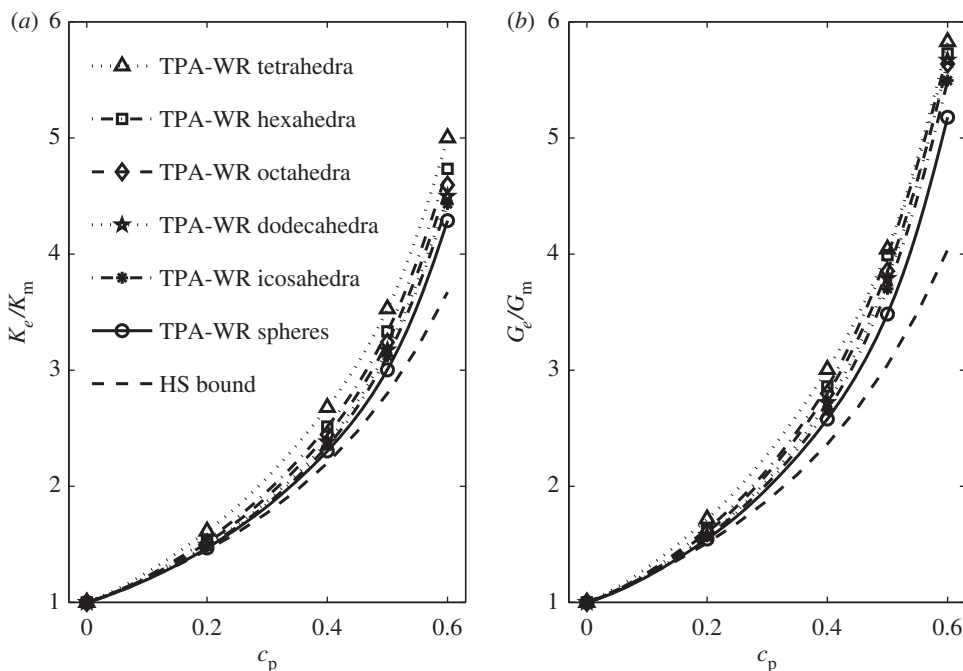


Figure 11. TPA of (a) bulk modulus and (b) shear modulus for isotropic systems of Platonic solids.

(figure 9a) and are capable to contact at large distances, $\beta_{12}/d > 1$, through V-V contact (figure 9b). This contact behaviour suggests that tetrahedra are near percolation compared to other packs, which leads to greater effective conductivity. This trend is also consistent with the percolation threshold, c_p^{per} , for systems of overlapping Platonic solids listed in table 4. This is the first time to the authors' knowledge that a shape effect has been predicted for isotropic systems with varying shapes up to high packing fractions using third-order statistical micromechanics. The resulting predictions of the thermal conductivity are also compared to the HS lower bound (see equation (B 1)) that is unable to capture any shape effect.

The TPA of the effective bulk modulus (equation (A 2)) and shear modulus (equation (A 5)) are presented in figure 11a,b, respectively. The same shape effect trend seen for the effective thermal conductivity is exhibited for both the shear and bulk moduli. However, the magnitude is less pronounced. With tetrahedra for example (dotted line with triangular markers), the normalized effective bulk modulus (K_e/K_m) for $c_p = 0.6$ is 5.00. In comparison to the pack of spheres ($K_e/K_m = 4.29$), the effective bulk modulus increases by 1.16 times (16.6% increase). Meanwhile, the normalized effective shear modulus (G_e/G_m) at $c_p = 0.6$ for the pack of tetrahedra increases by 1.13 times (12.6% increase) above the system of spheres. This indicates that the effective elastic properties are less sensitive to the inclusion shape. These predictions are also compared to the HS lower bounds (see equations (B 2) and (B 3)).

5. Conclusion

In this work, we predict with high accuracy thermal conductivity and elastic constants of isotropic packs of Platonic solids (crystalline materials). Verification studies are conducted for systems of overlapping and hard monodisperse spheres, and numerical approaches are found very accurate. Good agreement is shown between the third-order models and finite-element simulations for rigid particles in a deformable matrix, and the TPA using the WR microstructural parameters ζ_p and η_p is improved.

For the first time, TPAs of the thermal–mechanical properties are computed for isotropic systems of Platonic solids at various volume fractions. A significant particle shape effect is predicted for thermal conductivity, whereas the effective elastic moduli are less sensitive to the microstructural configuration. Based on our statistical framework, a large class of materials with arbitrary inclusion shapes can now be easily studied. Moreover, image-based modelling, using micro-computed tomography for example, can now be successfully employed for real material systems.

Funding statement. A.G. and K.M. acknowledge support from the Department of Energy, National Nuclear Security Administration, under award no. DE-NA0002377, and from Multiscale Design Systems, LLC under the contract no. FA8651-14-C-0045 (Eglin Air Force Base, STTR Phase II project) by the Department of Defense. T.L.J. was supported in part by the U.S. Department of Energy, National Nuclear Security Administration, Advanced Simulation and Computing Program, as a Cooperative Agreement under the Predictive Science Academic Alliance Program, under contract no. DE-NA0002378. G.A. and T.L.J. were also supported in part by the Defense Threat Reduction Agency, Basic Research award no. HDTRA1-13-0010 to University of Illinois, and T.L.J. in part by HDTRA1-14-1-0031 to University of Florida; Dr Suhithi Peiris, program manager.

Author contributions. A.G. developed the numerical integration/interpolation and statistical sampling methods, conducted numerical experiments and performed subsequent analysis of results. G.A. and T.J. developed the packing algorithm for Platonic solids. K.M. conceived and coordinated the studies, and contributed to analysis of results. A.G. and K.M. drafted the manuscript. All authors approved manuscript for publication.

Conflict of interests. The authors have no competing interests.

Appendix A. Third-order estimates for elastic constants

The parameters \mathcal{E}_L and \mathcal{E}_{UI} presented in equation (2.19) are defined as

$$\left. \begin{aligned} \mathcal{E}_L &= \frac{(128\zeta_m/K_m + 128\zeta_p/K_p + 99\zeta_m/G_m + 99\zeta_p/G_p) + 45(\eta_m/G_m + \eta_p/G_p)}{30(\zeta_m/G_m + \zeta_p/G_p)(6\zeta_m/K_m + 6\zeta_p/K_p - \zeta_m/G_m - \zeta_p/G_p) \cdots} \\ &\quad + 6(\eta_m/G_m + \eta_p/G_p)(2\zeta_m/K_m + 2\zeta_p/K_p + 21\zeta_m/G_m + 21\zeta_p/G_p) \end{aligned} \right\} \quad (\text{A } 1)$$

and

$$\mathcal{E}_{UI} = \frac{3(G_m\eta_m + G_p\eta_p)(6K_m\zeta_m + 6K_p\zeta_p + 7G_m\zeta_m + 7G_p\zeta_p) - 5(G_m\zeta_m + G_p\zeta_p)^2}{6(2K_m\zeta_m + 2K_p\zeta_p - G_m\zeta_m - G_p\zeta_p) + 30(G_m\eta_m + G_p\eta_p)}.$$

The TPA for the bulk and shear modulus of a two-phase isotropic material were derived by Torquato [52,53]. These approximations were simplified assuming stiff particles in a deformable matrix ($K_p/K_m = \infty$ and $G_p/G_m = \infty$). The bulk modulus is given as

$$\frac{K_e}{K_m} = \frac{1 + (4G_m/3K_m)K_{pm}c_p - (10G_m/(3K_m + 6G_m))K_{pm}G_{pm}c_m\zeta_p}{1 - K_{pm}c_p - (10G_m/(3K_m + 6G_m))K_{pm}G_{pm}c_m\zeta_p}, \quad (\text{A } 2)$$

where

$$K_{pm} = \frac{K_p - K_m}{K_p + (4/3)G_m} \quad (\text{A } 3)$$

and

$$G_{pm} = \frac{G_p - G_m}{G_p + G_m((9K_m + 8G_m)/(6K_m + 12G_m))}. \quad (\text{A } 4)$$

The TPA of the shear modulus for an infinite contrast is

$$\frac{G_e}{G_m} = \frac{1 + ((9K_m + 8G_m)/(6K_m + 12G_m))G_{pm}c_p - (2K_{pm}G_{pm}G_m/(3K_m + 6G_m))c_m\zeta_p \cdots}{1 - G_{pm}c_p - (2K_{pm}G_{pm}G_m/(3K_m + 6G_m))c_m\zeta_p \cdots} \cdot \frac{-G_{pm}^2/6\{[(3K_m + G_m)/(K_m + 2G_m)]^2c_m\eta_p + 5G_m[(2K_m + 3G_m)/(K_m + 2G_m)]^2c_m\zeta_p\}}{-G_{pm}^2/6\{[(3K_m + G_m)/(K_m + 2G_m)]^2c_m\eta_p + 5G_m[(2K_m + 3G_m)/(K_m + 2G_m)]^2c_m\zeta_p\}} \quad (\text{A } 5)$$

Appendix B. Hashin–Shtrikman bounds

The HS lower bound for the effective thermal conductivity [21] of an isotropic two-phase composite is given as

$$\frac{\kappa_e}{\kappa_m} = c_m \kappa_m + c_p \kappa_p - \frac{c_m c_p (\kappa_p - \kappa_m)^2}{c_m \kappa_p + c_p \kappa_m + 2\kappa_m}. \quad (\text{B } 1)$$

The HS lower bounds for the effective bulk and shear modulus [22] are defined as

$$\frac{K_e}{K_m} = c_m K_m + c_p K_p - \frac{c_m c_p (K_p - K_m)^2}{c_m K_p + c_p K_m + 4G_m/3} \quad (\text{B } 2)$$

and

$$\frac{G_e}{G_m} = c_m G_m + c_p G_p - \frac{c_m c_p (G_p - G_m)^2}{c_m G_p + c_p G_m + G_m((3K_m/2 + 4G_m/3)/(K_m + 2G_m))}, \quad (\text{B } 3)$$

respectively.

References

1. Srolovitz D, Egami T, Vitek V. 1981 Radial distribution function and structural relaxation in amorphous solids. *Phys. Rev. B* **24**, 6936–6944. (doi:10.1103/PhysRevB.24.6936)
2. Wooten F, Winer K, Weaire D. 1985 Computer generation of structural models of amorphous Si and Ge. *Phys. Rev. Lett.* **54**, 1392–1395. (doi:10.1103/PhysRevLett.54.1392)
3. Torquato S. 2002 *Random heterogeneous materials: microstructure and macroscopic properties*, vol. 16. New York, NY: Springer.
4. Nemat-Nasser S, Hori M. 1999 *Micromechanics: overall properties of heterogeneous materials*, vol. 2. Amsterdam, The Netherlands: Elsevier
5. Totsuji H, Kihara T. 1969 The correlation function for the distribution of galaxies. *Publ. Astron. Soc. Jpn* **21**, 221.
6. Eriksen HK, Hansen FK, Banday AJ, Górski KM, Lilje P. 2004 Asymmetries in the cosmic microwave background anisotropy field. *Astrophys. J.* **605**, 14–20. (doi:10.1086/382267)
7. Wiaux Y, Vielva P, Martinez-Gonzalez E, Vandergheynst P. 2006 Global universe anisotropy probed by the alignment of structures in the cosmic microwave background. *Phys. Rev. Lett.* **96**, 151303. (doi:10.1103/PhysRevLett.96.151303)
8. Gillman A, Matouš K, Atkinson S. 2013 Microstructure-statistics-property relations of anisotropic polydisperse particulate composites using tomography. *Phys. Rev. E* **87**, 022208. (doi:10.1103/PhysRevE.87.022208)
9. Bernal J. 1959 A geometrical approach to the structure of liquids. *Nature* **183**, 141–147. (doi:10.1038/183141a0)
10. Frisch H, Stillinger F. 1963 Contribution to the statistical geometric basis of radiation scattering. *J. Chem. Phys.* **38**, 2200–2207. (doi:10.1063/1.1733950)
11. Schmalzing J, Górski KM. 1998 Minkowski functionals used in the morphological analysis of cosmic microwave background anisotropy maps. *Mon. Not. R. Astron. Soc.* **297**, 355–365. (doi:10.1046/j.1365-8711.1998.01467.x)
12. Wochner P *et al.* 2009 X-ray cross correlation analysis uncovers hidden local symmetries in disordered matter. *Proc. Natl Acad. Sci. USA* **106**, 11 511–11 514. (doi:10.1073/pnas.0905337106)
13. Berkowitz B. 2002 Characterizing flow and transport in fractured geological media: a review. *Adv. Water Resour.* **25**, 861–884. (doi:10.1016/S0309-1708(02)00042-8)
14. Sun Z, Garboczi EJ, Shah SP. 2007 Modeling the elastic properties of concrete composites: experiment, differential effective medium theory, and numerical simulation. *Cement Concrete Compos.* **29**, 22–38. (doi:10.1016/j.cemconcomp.2006.07.020)
15. Li Y, Wong C. 2006 Recent advances of conductive adhesives as a lead-free alternative in electronic packaging: materials, processing, reliability and applications. *Mater. Sci. Eng. R Rep.* **51**, 1–35. (doi:10.1016/j.mser.2006.01.001)
16. Timofeeva EV, Routbort JL, Singh D. 2009 Particle shape effects on thermophysical properties of alumina nanofluids. *J. Appl. Phys.* **106**, 014304. (doi:10.1063/1.3155999)
17. Yvonnet J, He QC, Toulemonde C. 2008 Numerical modelling of the effective conductivities of composites with arbitrarily shaped inclusions and highly conducting interface. *Compos. Sci. Technol.* **68**, 2818–2825. (doi:10.1016/j.compscitech.2008.06.008)

18. Yvonnet J, Quang HL, He QC. 2008 An XFEM/level set approach to modelling surface/interface effects and to computing the size-dependent effective properties of nanocomposites. *Comput. Mech.* **42**, 119–131. (doi:10.1007/s00466-008-0241-y)
19. Chauhan D, Singhvi N, Singh R. 2012 Effect of geometry of filler particles on the effective thermal conductivity of two-phase systems. *Int. J. Mod. Nonlinear Theory Appl.* **1**, 40–46. (doi:10.4236/ijmnta.2012.12005)
20. Brown Jr WF. 1955 Solid mixture permittivities. *J. Chem. Phys.* **23**, 1514–1517. (doi:10.1063/1.1742339)
21. Hashin Z, Shtrikman S. 1962 A variational approach to the theory of the effective magnetic permeability of multiphase materials. *J. Appl. Phys.* **33**, 3125–3131. (doi:10.1063/1.1728579)
22. Hashin Z, Shtrikman S. 1963 A variational approach to the theory of the elastic behaviour of multiphase materials. *J. Mech. Phys. Solids* **11**, 127–140. (doi:10.1016/0022-5096(63)90060-7)
23. Beran M. 1965 Use of the vibrational approach to determine bounds for the effective permittivity in random media. *Il Nuovo Cimento Ser. 10* **38**, 771–782. (doi:10.1007/BF02748596)
24. Torquato S 1980 Microscopic approach to transport in two-phase random media. PhD thesis, State University of New York at Stony Brook.
25. Milton GW. 1981 Bounds on the electromagnetic, elastic, and other properties of two-component composites. *Phys. Rev. Lett.* **46**, 542–545. (doi:10.1103/PhysRevLett.46.542)
26. Beran M, Molyneux J. 1966 Use of classical variational principles to determine bounds for the effective bulk modulus in heterogeneous media. *Q. Appl. Math.* **24**, 107–118.
27. McCoy JJ. 1970 On the displacement field in an elastic medium with random variations of material properties. *Recent Adv. Eng. Sci.* **5**, 235–254.
28. Milton G, Phan-Thien N. 1982 New bounds on effective elastic moduli of two-component materials. *Proc. R. Soc. Lond. A* **380**, 305–331. (doi:10.1098/rspa.1982.0044)
29. Castañeda PP. 1998 Three-point bounds and other estimates for strongly nonlinear composites. *Phys. Rev. B* **57**, 12077–12083. (doi:10.1103/PhysRevB.57.12077)
30. Torquato S, Rintoul M. 1995 Effect of the interface on the properties of composite media. *Phys. Rev. Lett.* **75**, 4067–4070. (doi:10.1103/PhysRevLett.75.4067)
31. Berryman JG. 1985 Variational bounds on elastic constants for the penetrable sphere model. *J. Phys. D Appl. Phys.* **18**, 585–597. (doi:10.1088/0022-3727/18/4/003)
32. Berryman JG. 1988 Interpolating and integrating three-point correlation functions on a lattice. *Journal of Computational Physics* **75**, 86–102. (doi:10.1016/0021-9991(88)90100-3)
33. Corson PB. 1974 Correlation functions for predicting properties of heterogeneous materials. II. Empirical construction of spatial correlation functions for two-phase solids. *J. Appl. Phys.* **45**, 3165–3170. (doi:10.1063/1.1663742)
34. Helte A. 1995 Fourth-order bounds on the effective bulk and shear moduli of random dispersions of penetrable spheres. *Proc. R. Soc. Lond. A* **450**, 651–665. (doi:10.1098/rspa.1995.0105)
35. Helsing J. 1995 Estimating effective properties of composites from cross-sectional photographs. *J. Comput. Phys.* **117**, 281–288. (doi:10.1006/jcph.1995.1066)
36. Berryman JG. 1985 Measurement of spatial correlation functions using image processing techniques. *J. Appl. Phys.* **57**, 2374–2384. (doi:10.1063/1.334346)
37. Coker DA, Torquato S, Dunsmuir JH. 1996 Morphology and physical properties of Fontainebleau sandstone via a tomographic analysis. *J. Geophys. Res. Solid Earth* **101**, 17 497–17 506. (doi:10.1029/96JB00811)
38. Beasley J, Torquato S. 1986 Bounds on the conductivity of a suspension of random impenetrable spheres. *J. Appl. Phys.* **60**, 3576–3581. (doi:10.1063/1.337614)
39. Torquato S, Lado F. 1986 Effective properties of two-phase disordered composite media. II. Evaluation of bounds on the conductivity and bulk modulus of dispersions of impenetrable spheres. *Phys. Rev. B* **33**, 6428. (doi:10.1103/PhysRevB.33.6428)
40. Miller C, Torquato S. 1990 Effective conductivity of hard-sphere dispersions. *J. Appl. Phys.* **68**, 5486–5493. (doi:10.1063/1.347007)
41. Liasneuski H, Hlushkou D, Khirevich S, Hötzel A, Tallarek U, Torquato S. 2014 Impact of microstructure on the effective diffusivity in random packings of hard spheres. *J. Appl. Phys.* **116**, 034904. (doi:10.1063/1.4889821)
42. Gillman A, Matouš K. 2014 Third-order model of thermal conductivity for random polydisperse particulate materials using well-resolved statistical descriptions from tomography. *Phys. Lett. A* **378**, 3070–3073. (doi:10.1016/j.physleta.2014.08.032)

43. Skoge M, Donev A, Stillinger FH, Torquato S. 2006 Packing hyperspheres in high-dimensional Euclidean spaces. *Phys. Rev. E* **74**, 041127. (doi:10.1103/PhysRevE.74.041127)
44. Lubachevsky BD, Stillinger FH. 1990 Geometric properties of random disk packings. *J. Stat. Phys.* **60**, 561–583. (doi:10.1007/BF01025983)
45. Donev A, Torquato S, Stillinger FH. 2005 Neighbor list collision-driven molecular dynamics simulation for nonspherical hard particles. I. Algorithmic details. *J. Comput. Phys.* **202**, 737–764. (doi:10.1016/j.jcp.2004.08.014)
46. Lee H, Brandyberry M, Tudor A, Matouš K. 2009 Three-dimensional reconstruction of statistically optimal unit cells of polydisperse particulate composites from microtopography. *Phys. Rev. E* **80**, 061301–1. (doi:10.1103/PhysRevE.80.061301)
47. Lee H, Gillman AS, Matouš K. 2011 Computing overall elastic constants of polydisperse particulate composites from microtomographic data. *J. Mech. Phys. Solids* **59**, 1838–1857. (doi:10.1016/j.jmps.2011.05.010)
48. Milton GW. 2002 *The theory of composites*, vol. 6. Cambridge, UK: Cambridge University Press.
49. Torquato S. 1985 Effective electrical conductivity of two-phase disordered composite media. *J. Appl. Phys.* **58**, 3790–3797. (doi:10.1063/1.335593)
50. Kim IC, Torquato S. 1991 Effective conductivity of suspensions of hard spheres by Brownian motion simulation. *J. Appl. Phys.* **69**, 2280–2289. (doi:10.1063/1.348708)
51. Gibiansky L, Torquato S. 1995 Geometrical-parameter bounds on the effective moduli of composites. *J. Mech. Phys. Solids* **43**, 1587–1613. (doi:10.1016/0022-5096(95)00049-O)
52. Torquato S. 1997 Effective stiffness tensor of composite media. I. Exact series expansions. *J. Mech. Phys. Solids* **45**, 1421–1448. (doi:10.1016/S0022-5096(97)00019-7)
53. Torquato S. 1998 Effective stiffness tensor of composite media. II. Applications to isotropic dispersions. *J. Mech. Phys. Solids* **46**, 1411–1440. (doi:10.1016/S0022-5096(97)00083-5)
54. Coker DA, Torquato S. 1995 Extraction of morphological quantities from a digitized medium. *J. Appl. Phys.* **77**, 6087–6099. (doi:10.1063/1.359134)
55. Genz A. 1987 A package for testing multiple integration subroutines. In *Numerical integration* (eds P Keast, G Fairweather), pp. 337–340. New York, NY: Springer.
56. The CGAL Project. 2014 CGAL User and Reference Manual. 4.5 ed. CGAL Editorial Board. See <http://doc.cgal.org/4.5/Manual/packages.html>.
57. Hert S, Seel M. 2014 dD Convex Hulls and Delaunay Triangulations. CGAL User and Reference Manual. 4.5 ed. CGAL Editorial Board. See <http://doc.cgal.org/4.5/Manual/packages.html#PkgConvexHullDSummary>.
58. Rocchini C, Cignoni P. 2000 Generating random points in a tetrahedron. *J. Graph. Tools* **5**, 9–12.
59. Torquato S, Lado F, Smith PA. 1987 Bulk properties of two-phase disordered media. IV. Mechanical properties of suspensions of penetrable spheres at nondilute concentrations. *J. Chem. Phys.* **86**, 6388–6392. (doi:10.1063/1.452427)
60. Segurado J, Llorca J. 2002 A numerical approximation to the elastic properties of sphere-reinforced composites. *J. Mech. Phys. Solids* **50**, 2107–2121. (doi:10.1016/S0022-5096(02)00021-2)
61. Maggi F, Stafford S, Jackson T, Buckmaster J. 2008 Nature of packs used in propellant modeling. *Phys. Rev. E* **77**, 046107. (doi:10.1103/PhysRevE.77.046107)
62. Stafford DS, Jackson TL. 2010 Using level sets for creating virtual random packs of non-spherical convex shapes. *J. Comput. Phys.* **229**, 3295–3315. (doi:10.1016/j.jcp.2010.01.003)
63. Amadio G 2014 Particle packings and microstructure modeling of energetic materials. PhD thesis, University of Illinois, Urbana, IL, USA.
64. Torquato S, Jiao Y. 2009 Dense packings of the Platonic and Archimedean solids. *Nature* **460**, 876–879. (doi:10.1038/nature08239)
65. Torquato S, Jiao Y. 2009 Dense packings of polyhedra: platonic and archimedean solids. *Phys. Rev. E* **80**, 041104. (doi:10.1103/PhysRevE.80.041104)
66. Torquato S, Jiao Y. 2013 Effect of dimensionality on the percolation threshold of overlapping nonspherical hyperparticles. *Phys. Rev. E* **87**, 022111. (doi:10.1103/PhysRevE.87.022111)